






Article

Effect of Au Plasmonic Material on Poly M-Toluidine for Photoelectrochemical Hydrogen Generation from Sewage Water

Ahmed Adel A. Abdelazeez ¹, N.M.A. Hadia ^{2,3,*}, Abdel-Hamid I. Mourad ^{4,5,*}, Gehad Abd El-Fatah ⁶, Mohamed Shaban ^{7,8}, Ashour M. Ahmed ⁷, Meshal Alzaid ², Nizamudeen Cherupurakal ⁴ and Mohamed Rabia ^{6,7}

- ¹ Nanoscale Science, Chemistry Department, University of North Carolina at Charlotte, Charlotte, NC 28223, USA; aabdelh2@uncc.edu
- ² Physics Department, College of Science, Jouf University, Al-Jouf, Sakaka P.O. Box 2014, Saudi Arabia; mmalzaid@ju.edu.sa
- ³ Basic Sciences Research Unit, Jouf University, Sakaka P.O. Box 2014, Saudi Arabia
- ⁴ Mechanical and Aerospace Engineering Department, College of Engineering, United Arab Emirates University, Al Ain 15551, United Arab Emirates; 201890121@uaeu.ac.ae
- ⁵ Mechanical Design Department, Faculty of Engineering, Helwan University, Cairo 11795, Egypt
- ⁶ Nanomaterials Science Research Laboratory, Chemistry Department, Faculty of Science, Beni-Suef University, Beni Suef 62514, Egypt; gehad.abdelfattah1508@science.bsu.edu.eg (G.A.E.-F); mohamedchem@science.bsu.edu.eg (M.R.)
- ⁷ Nanophotonics and Applications Lab, Physics Department, Faculty of Science, Beni-Suef University, Beni Suef 62514, Egypt; mssfadel@aucegypt.edu (M.S.); ashour.elshemey@gmail.com (A.M.A.)
- ⁸ Physics Department, Faculty of Science, Islamic University of Madinah, P.O. Box 170, Madinah 42351, Saudi Arabia
- * Correspondence: nmhadia@ju.edu.sa (N.M.A.H.); ahmourad@uaeu.ac.ae (A.-H.I.M.)



Citation: Abdelazeez, A.A.A.; Hadia, N.M.A.; Mourad, A.-H.I.; El-Fatah, G.A.; Shaban, M.; Ahmed, A.M.; Alzaid, M.; Cherupurakal, N.; Rabia, M. Effect of Au Plasmonic Material on Poly M-Toluidine for Photoelectrochemical Hydrogen Generation from Sewage Water. *Polymers* **2022**, *14*, 768. <https://doi.org/10.3390/polym14040768>

Academic Editor: Mohammad Afsar Uddin

Received: 25 January 2022

Accepted: 7 February 2022

Published: 16 February 2022

Publisher's Note: MDPI stays neutral with regard to jurisdictional claims in published maps and institutional affiliations.

Abstract: This study provides H₂ gas as a renewable energy source from sewage water splitting reaction using a PMT/Au photocathode. So, this study has a dual benefit for hydrogen generation; at the same time, it removes the contaminations of sewage water. The preparation of the PMT is carried out through the polymerization process from an acid medium. Then, the Au sputter was carried out using the sputter device under different times (1 and 2 min) for PMT/Au-1 min and PMT/Au-2min, respectively. The complete analyses confirm the chemical structure, such as XRD, FTIR, HNMR, SEM, and Vis-UV optical analyses. The prepared electrode PMT/Au is used for the hydrogen generation reaction using Na₂S₂O₃ or sewage water as an electrolyte. The PMT crystalline size is 15 nm. The incident photon to current efficiency (IPCE) efficiency increases from 2.3 to 3.6% (at 390 nm), and the number of H₂ moles increases from 8.4 to 33.1 mmol h⁻¹ cm⁻² for using Na₂S₂O₃ and sewage water as electrolyte, respectively. Moreover, all the thermodynamic parameters, such as activation energy (*E_a*), enthalpy (ΔH^*), and entropy (ΔS^*), were calculated; additionally, a simple mechanism is mentioned for the water-splitting reaction.

Keywords: poly(m toluidine); photocatalyst; water splitting; photoelectrochemical H₂ generation; plasmonic Au nanoparticles; sewage water



Copyright: © 2022 by the authors. Licensee MDPI, Basel, Switzerland. This article is an open access article distributed under the terms and conditions of the Creative Commons Attribution (CC BY) license (<https://creativecommons.org/licenses/by/4.0/>).

1. Introduction

Fossil fuels, such as petroleum, oil, and natural gas, represent an essential energy source. The leakage of these sources and the contaminations of gases exhausts, SO_x, NO_x, and CO_x, push scientists worldwide to think about a replaceable energy source, which is represented by renewable energy sources [1–3]. These renewable energy sources have advantages represented in clean energy and sustainability [4–6].

Hydrogen gas represents the primary solar energy source produced under the water-splitting reaction [7,8]. Hydrogen gas has advantages in its high combustion and performance [9]. Moreover, water splitting is carried out using photocatalytic materials under

the light, thus decreasing the voltage used for this reaction. The photocatalytic materials must be semiconductor materials that can form electron–hole pairs, in which the electrons are formed to represent the produced current density values. With the increase in the surface area, the produced J_{ph} values increase. So, the photocatalytic materials with nanowires, nanotubes, and nanosheets have the optimum properties for the hydrogen generation process [10]. Although metal oxides, sulfide, and nitrides represent suitable catalytic materials, low hydrogen rates and complex preparation methods limit the use of such semiconductor materials [11–14].

The effect of noble metals, such as Pt, Rh, and Au, on semiconductor materials for hydrogen generation was studied by different researchers [15]. These noble metals have a plasmonic effect that causes photon capture and electron resonance on the neighboring semiconductor materials [16]. Shi et al. [17] studied the CdS/Pt photocatalytic reaction for hydrogen generation using a Xe lamp. Zhao et al. [18] studied the TiO₂-Au-CdS photocatalyst reaction under 300 W Xe, in which the Au nanomaterials activate the surface of CdS and TiO₂ and cause energy transfer between them.

Polymeric nanomaterials, such as aniline and its derivatives, are replaceable sources of materials with high advantages, especially their easy preparation, low cost, high stability, and reproducibility [19,20]. Moreover, these polymer materials have great optical properties that qualify them as high efficient photocatalytic materials [21,22].

There have been some studies carried out on these polymer materials for photocatalytic applications and some methods have been proposed for preparing photocatalytic polymers, such as chemical, electrochemical, and electrospun methods [23–26].

Ghosh et al. [27] studied thiophene polymers (poly(3,4-ethylene dioxathiophene)) as catalytic materials for contamination decomposition. Yin et al. [28] studied poly(diphenyl butadiyne) for pollution removal from fiber materials. Ramohlola et al. [29] studied poly(3-aminobenzoic acid) for H₂ production through a H₂SO₄ electrolyte with J_{ph} of 0.13 mA cm⁻². Some studies have been carried out for testing WS₂/polythiophene/Au or Ni/PANI as photocatalytic materials [28,30]. Belabed et al. [31] studied PANI/TiO₂ for hydrogen generation under artificial light 200 W lamp.

Poly(m-toluidine) (PMT) is a promising polymer with great properties, especially its highly efficient optical absorbance and excellent electrical behavior. Additional advantages are its high environmental compatibility, reproducibility, and stability [24]. There are few studies carried out with this material as a photocatalytic electrode for water splitting.

The previous literature has studied hydrogen generation under water-splitting reactions, but the hydrogen generation rate is still very small. Additionally, the previous studies use a sacrificing agent for the hydrogen generation; sometimes these materials, such as H₂SO₄ or NaOH, with very low or high pH values cause corrosion in the electrodes. Moreover, the previous studies usually use freshwater as a source of hydrogen with the leakage of this water for drinking.

This study prepares PMT, PMT/Au-1 min, and PMT/Au-2 min nanomaterials and characterizes them well using different analytical tools. PMT/Au-2 min is used as an electrode for hydrogen generation from sewage water with high efficiency and low cost. The hydrogen rate is compared with Na₂S₂O₃ electrolytes. The effect of light wavelengths, stability, and temperature are studied. The thermodynamic parameters and hydrogen moles are calculated using different electrolyte sewage water or Na₂S₂O₃.

2. Experimental Part

2.1. Materials

M-Toluidine (MT) was obtained from VEB Laborchemie Apolda, Germany. Acetone, H₂SO₄, Na₂SO₄, and Na₂S₂O₃ were purchased from Adwic Company, Cairo, Egypt. ITO glass was obtained from VWR Company, Darmstadt, Germany.

2.2. Electropolymerization of MT and Preparation of the Electrode

A potentiodynamic technique in the three-electrode cell was performed in the electropolymerization phase of MT to form PMT, as defined in our previous study [32]. The electropolymerization reaction was carried out on ITO glass ($20\ \Omega$) through the anodic polymerization reaction using Potentiostat/Galvanostat Wenking (PGS 95), Hubertusstr, Germany. ITO, PT, and calomel represent the working, counter, and reference electrodes, respectively. During the electropolymerization process, Na_2SO_4 and H_2SO_4 were used as electrolyte and acid medium, respectively. The electropolymerization reaction was carried out from 0.4 to +1500 mV (in the positive direction) with a scan rate of $40\ \text{mVs}^{-1}$. The thickness of the PMT was determined through 10 cyclic voltammetry runs on ITO, then the film was rinsed in water and dried at $60\ ^\circ\text{C}$ for 12 h.

The sputter coating of the Au was carried out from Au disc (99.99%) using a sputter coating device for 1 and 2 min on the surface of PMT for PMT/Au-1 min and PMT/Au-2 min, respectively.

This electrode was then used for hydrogen generation from sewage water or $\text{Na}_2\text{S}_2\text{O}_3$ solution, and the results of both electrolytes were compared to each other. The hydrogen generation was carried out from a three-electrode cell, in which the PMT/Au-2 min was the working electrode. At the same time, graphite and calomel were the counter and reference electrodes, respectively.

2.3. Characterization Process

The prepared polymer and polymer/Au morphology were characterized using an X-ray diffractometer (XRD) device (X'Pert Pro, Almelo, The Netherlands) Almelo, the Netherlands, worked at 40 mA and 45 kV. FTIR-340 Jasco spectrophotometer, Easton, USA, was used for FTIR analyses. The $^1\text{H-NMR}$ measurement (the Varian EM 360 L NMR, Oberkochen, Germany) confirmed the functional groups in the polymer materials. Scanning electron microscopy was used to conduct morphological studies (ZEISS SUPRA Gemini Column, Oberkochen, Germany). Optical analyses of the prepared films were determined using the Shimadzu UV/Vis spectrophotometer (M160 PC, Waltham, MA, USA).

3. Results and Discussion

3.1. Electropolymerization of *m*-Toluidine

The electropolymerization process was carried out through the optimization of the conditions of the preparation, represented in the current J_p value. This J_p value represents the rate of the reaction [33].

The effect of the *m*-toluidine monomer 0.04 and 0.14 M study is shown in Figure 1A at $40\ \text{mVs}^{-1}$ and 303 K. The optimum concentration was 0.12 M, with an optimum J_p value. After the increase in the concentration to over 0.12 M, more collisions with the monomer take place, which cause the deactivation of the electrode surface [34]; this decreases the J_p value to 0.14 M.

In the same manner, the effect of H_2SO_4 from 0.1 to 0.6 M is shown in Figure 1B; the optimum concentration of H_2SO_4 is 0.5 M. Additionally, the effect of Na_2SO_4 from 0.025 to 0.1 M is shown in Figure 1C; the optimum concentration is 0.075 M. The effect of temperature from 278 to 303 K is shown in Figure 1D; the optimum temperature is 298 K. These conditions confirm that the optimum conditions for the preparation of PMT are 0.12 M *m*-toluidine, 0.5 M H_2SO_4 , and 0.075 M Na_2SO_4 at 298 K.

3.2. PMT and PMT/Au Analyses

The chemical construction of the PMT nanomaterials is shown in Figure 2a, and the data are summarized in Table 1. From the Figure and the Table, it can be observed that the PMT function groups appeared well, in which the C–H, N–H, and C–N function groups appeared at 3106 , 3429 , and $1339\ \text{cm}^{-1}$, respectively. C=C, benzenoid and quinoid appear at 1465 , 1407 , and $1631\ \text{cm}^{-1}$, respectively. The vibration of C–H in/out of the plan is localized at 1051 and $595\ \text{cm}^{-1}$, respectively. After the PANI/Au composite formation,

there are shifts in most of the PANI peaks (Figure 2a, red curve), which is related to the interaction between the functional groups and the Au nanoparticles.

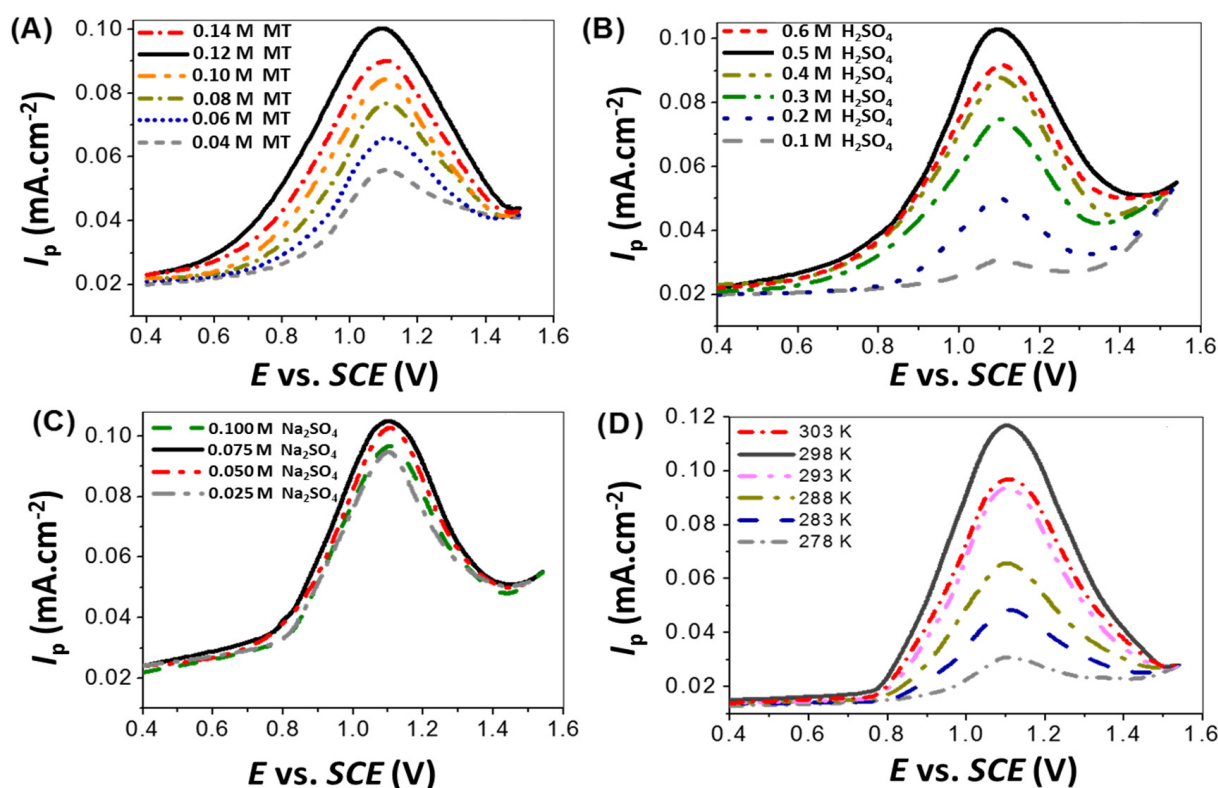


Figure 1. The effect of the concentrations of (A) m-toluidine (0.04 to 0.14 M), (B) H_2SO_4 (0.1 to 0.6 M), (C) Na_2SO_4 (0.025 to 0.1 M), and (D) temperature (278 to 303 K) on the electropolymerization of m-toluidine.

For more confirmation of the chemical structure of the PMT, an ^1H NMR analysis was carried out, as shown in Figure 2b. The protons related to the methyl and N-H group are located at signals $\delta = 1.23$ and 4.07 ppm, respectively. The benzene ring has signals from $\delta = 6.93$ to $\delta = 7.27$ ppm [35]. The summarized data are shown in Table 2.

To further confirm the chemical structure of PMT, PMT/Au-1 min, and PMT/Au-2 min, XRD analyses were carried out and the results are shown in Figure 2c. The PMT shows a broad peak at $2\theta = 25.55$, indicating the semi-crystalline nature of the polymer [40,41]. After the Au coating, this peak is more enhanced due to the composite formation; sharp peaks appear in this region with high intensity, which increases from Au coating 1 to 2 min. Moreover, there is an additional peak that appears at $2\theta = 38.3^\circ$ at growth direction (111); this peak increases in intensity for 1 and 2 min coating.

This confirms the growth of the composite with high crystallinity after the Au coating process [41]; this crystalline nature confirms the availability of the composite for water-splitting reaction with high efficiency [42].

Scherrer's formula [41] ($D = 0.9 \lambda / W \cos\theta$) was used to calculate the crystal size. This formula depends on the angle (θ) in radian, wavelength (λ), and the full width half maximum (W). From this formula, we calculated that the crystalline size of PMT is ~ 15 nm, and this crystalline size increases to 24 and 35 nm, after Au coating for 1 and 2 min, respectively. Additionally, the standard stick patterns for ITO/PMT/Au-1 min and ITO/PMT/Au-2 min are shown in Figure 2d,e, respectively.

The morphologies of the prepared PMT, PMT/Au-1 min, and PMT/Au-2 min are shown in Figure 3A–C, respectively. The PMT has a nanopore surface with a smooth lamellar behavior. The diameter of the particles is about 20–30 nm. After Au nanoparticle

coating for 1 and 2 min (sputter coating), the porous nature of the surface increased, which is caused by the increase in the active sites of the PMT/Au composite. The average particles sizes of Au nanoparticles for 1 and 2 min are ~15 and 38 nm, respectively. Increasing the Au coating to 3 min (Figure 3D) makes the surface completely blocked with the Au metals. So, these properties prevent the role of the PMT for additional photocatalytic applications.

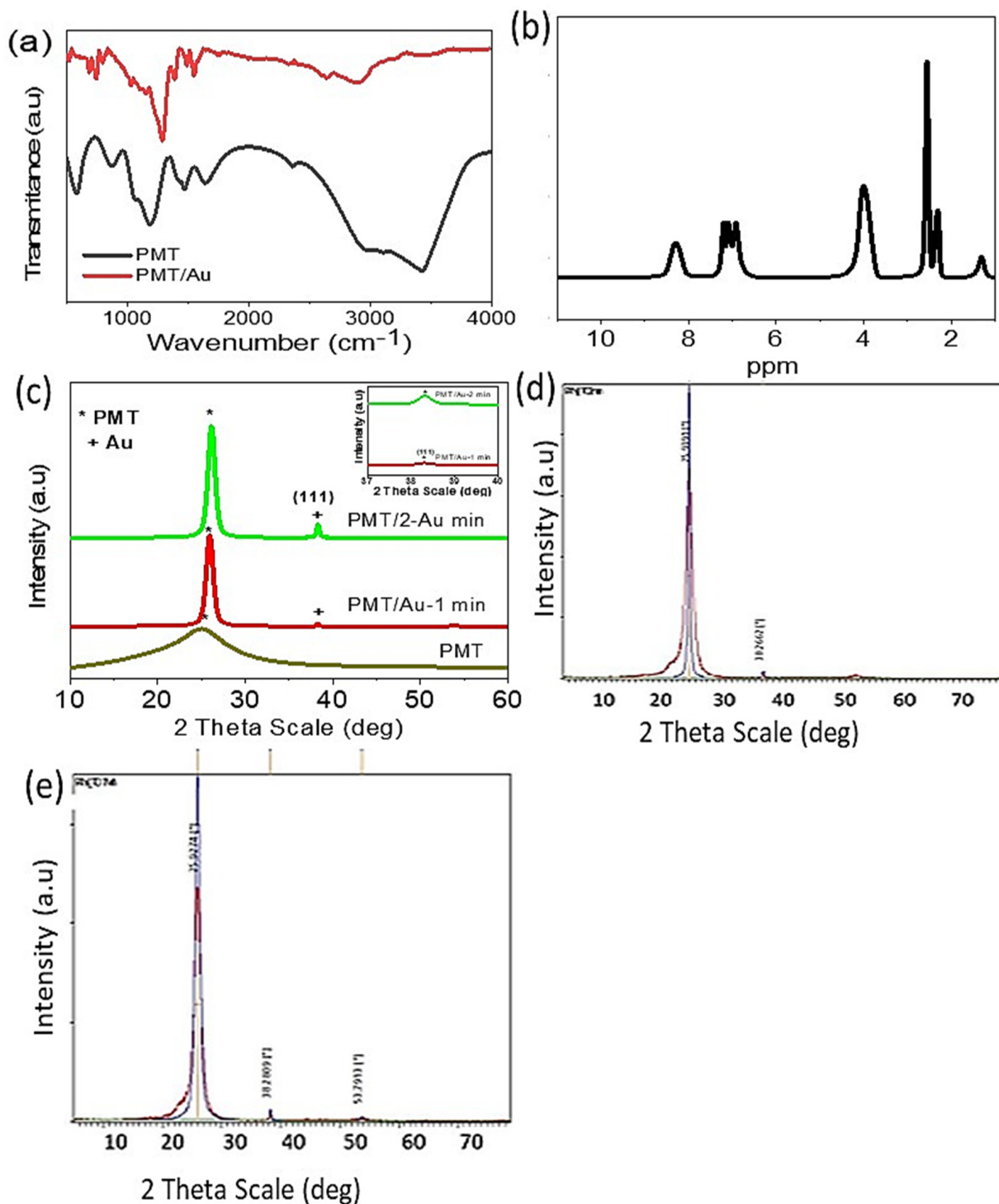


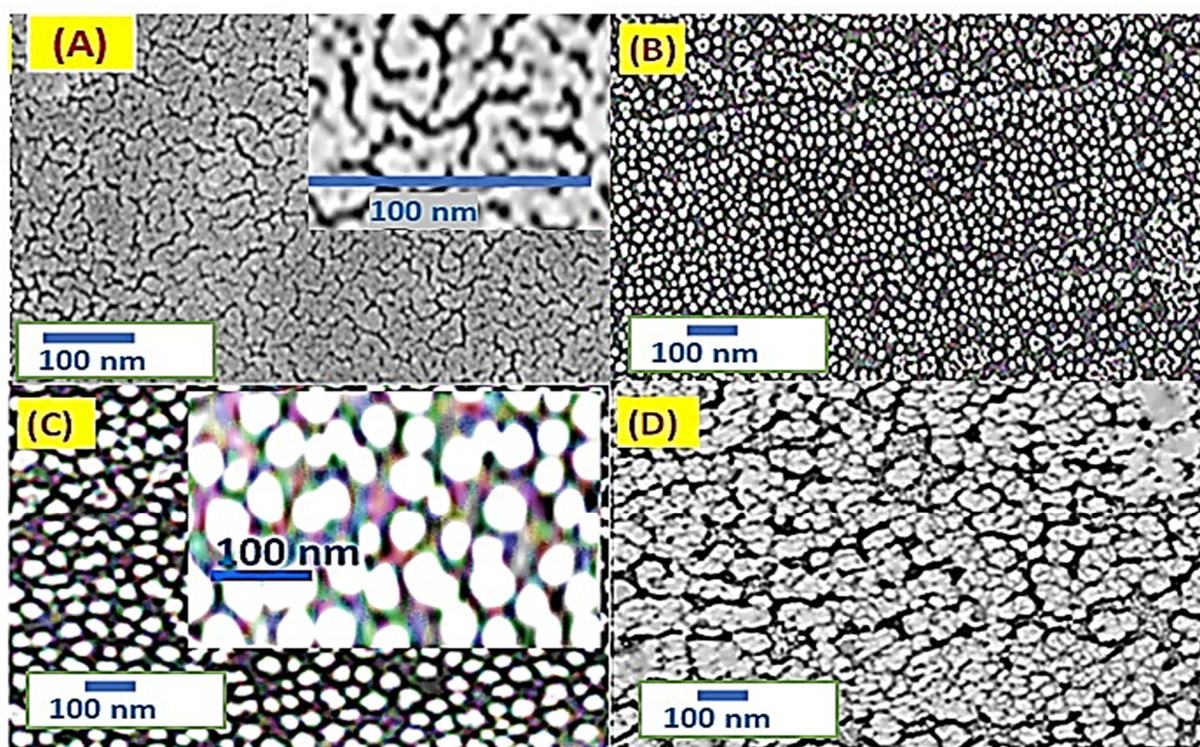
Figure 2. (a) FT-IR and (b) ¹H NMR of PMT. (c) XRD of PMT, PMT/Au-1 min and PMT/Au-2 min. (d,e) Standard stick pattern for ITO/PMT/Au-1 min and ITO/PMT/Au-2 min, respectively.

Table 1. The FT-IR analysis of the PMT nanomaterial.

Band Position (cm ⁻¹)	Assignment
3429	N–H group [35–37]
3106	Aromatic C–H group
2950	Methyl group stretching [32]
2357	Adsorbed H ₂ O or CO ₂ from the atmosphere [38]
1465 and 1407	C=C benzenoid [32]
1631	C=C quinoid
1339	C–N vibrations
1051	C–H in-plane
595	C–H out of plane
879	Aromatic rings para-disubstituted

Table 2. The summary of the HNMR analysis.

Chemical Shift (ppm)	Assignment and Structure
1.23	The proton of the methyl group [39]
2.56	DMSO proton (solvent) [35]
2.3	Adsorbed H ₂ O
4.07	Singlet signal for NH proton [35]
6.93 to 7.27	The protons of the benzene ring [39]

**Figure 3.** SEM images of PMT for Au coating with times of (A) 0, (B) 1, (C) 2, and (D) 3 min.

The PMT/Au-2 min has the optimum features for additional photocatalytic applications from these surface morphology properties.

These morphological properties are confirmed using the ImageJ program modeling as shown in Figure 4A–C, for PMT, PMT/Au-1 min, and PMT/Au-2 min, respectively. This program can calculate the cross-section and show the morphology well. From these figures, it can be observed that the PMT morphology is porous with uniform nature; this porosity and roughness increase after the Au coating process for 1 and 2 min. Moreover, the cross-section of the film increases with a Au coating from 1 to 2 min.

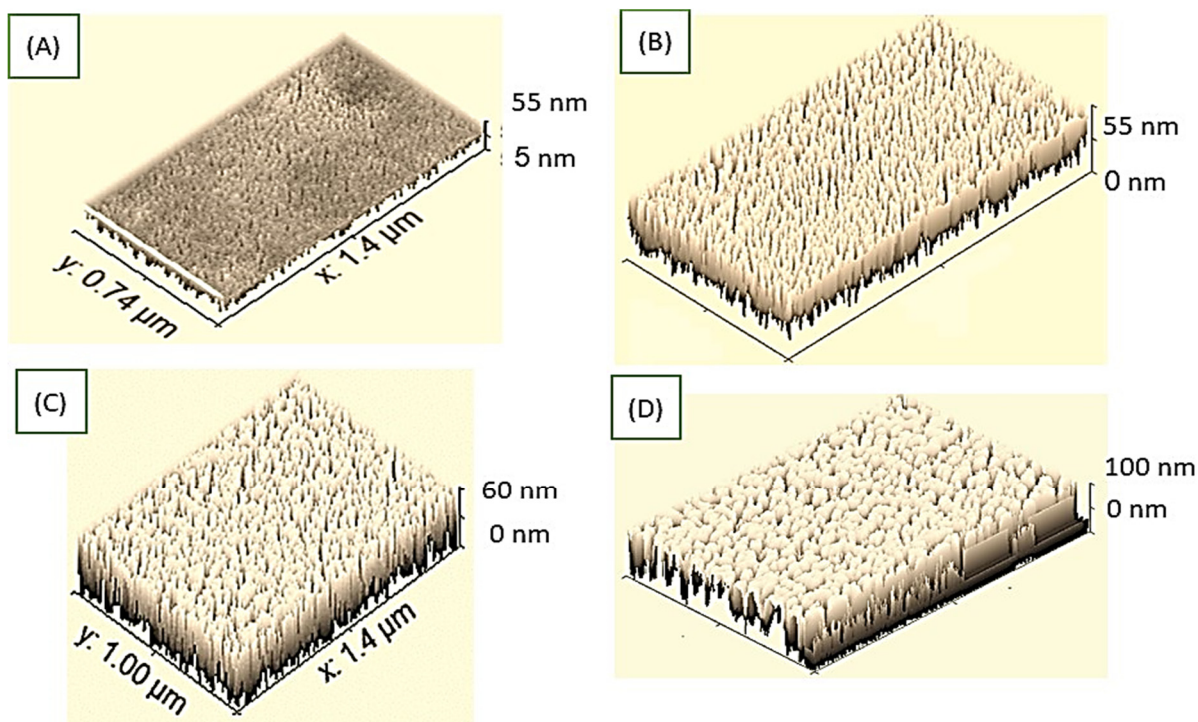


Figure 4. Roughness and cross-section using Image J program for PMT after Au coating for the times of (A) 0, (B) 1, (C) 2, and (D) 3 min.

By increasing the Au coating to 3 min, the Au nanoparticles completely block the PMT surface. This modeling study confirms the SEM image’s behavior.

The optical properties of the PMT, PMT/Au-1 min, and PMT/Au-2 min nanomaterials are shown in Figure 5A, and their bandgaps are shown in Figure 5B. From the absorbance curve, it can be observed that the PMT has two absorbance peaks in the UV and Vis regions at 265 and 550 nm, respectively. These peaks are related to the electrons’ transition from band to band and the polymer conjugations chains [41].

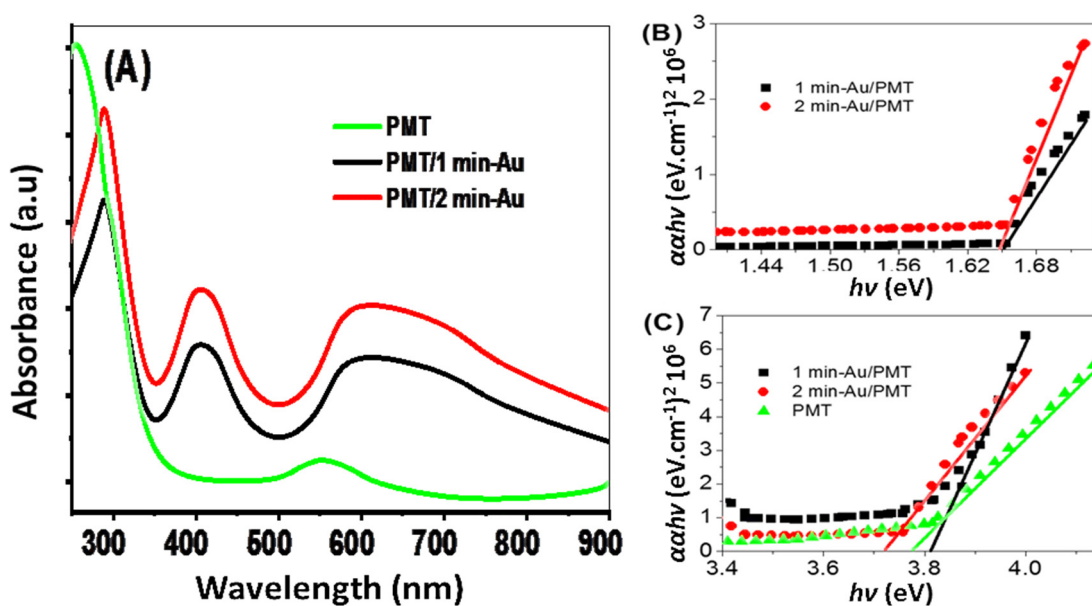


Figure 5. (A) The optical absorbance and (B,C) bandgap values for the PMT, PMT/Au-1 min, and PMT/Au-2 min nanomaterials.

After the Au sputter coating for 1 and 2 min, the optical absorbance increases, and the composite has three absorbance peaks, at 295 nm in the UV region and 430 and 605 nm in the Vis region. The peak at 605 nm is related to the plasmonic resonance of Au nanomaterials. After the formation of these three peaks, the composite has peaks that are over most of the optical regions in the UV, Vis, and near IR regions; these peaks have redshifts in wavelengths in comparison with the PMT absorbance.

The Au nanoparticles have a significant role in enhancing the optical properties of the composite. The main property of the Au NPs derives from dimensional confinement (sizes smaller than the wavelength of light), which leads to the alteration of their optical response following the appearance of a phenomenon called “surface plasmon resonance” (SPR), which fundamentally arises from the collective and coherent oscillation of the free conduction electrons in a continuous band structure, due to the resonant excitation caused by the incident photons or electromagnetic radiation [43,44]. This LPSR causes the free electrons of Au to oscillate coherently, creating a strong electric field on the Au nanoparticles. This field is transferred to the neighbor PMT semiconductor polymer for creating an electron–hole pair [45]. From this process, the electrons are collected on the surface and ready for an additional photocatalytic reaction and to create J_{ph} values. So, the PMT/Au-2 min nanocomposite is qualified to generate photoelectrochemical H₂ gas under the water-splitting reaction.

The bandgaps (E_g) for the PMT, PMT/Au-1 min, and PMT/Au-2 min were calculated from Tauc’s equations (Equations (1) and (2)) [46]. These equations are based on the absorbance (A), film thickness (d), absorbance coefficient (α), light frequency (ν), Boltzmann (B), and Planck (h) constants [47].

$$(\alpha h\nu)^2 = B (h\nu - E_g) \quad (1)$$

$$\alpha = \left(\frac{2303}{d} \right) A \quad (2)$$

From Tauc’s equation and Figure 5B,C, it can be observed that the bandgap of ITO/PMT is 3.74 eV for the wavelength 329.12 nm; this value agrees well with the previous literature [48]. After the Au sputter coating and the formation of the PMT/Au-1 min and PMT/Au-2 min, these two composites have bandgaps for the absorbance peaks in the near IR region at 1.64 and 1.63 eV, respectively (Figure 5B). Moreover, another bandgap is also related to the UV region peak at 3.8 and 3.70 eV (Figure 5C) for the two composites, respectively.

These absorbance and bandgap values for the PMT/Au-2 min confirm that this composite has the optimum optical properties compared to PMT or PMT/Au-1 min.

So, the photoelectrode based on this composite is qualified for photocatalytic applications and H₂ generation through the water-splitting reaction.

3.3. Electrochemical Hydrogen Generation

The electrochemical H₂ generation reaction was carried out through the three-electrode cell, in which the prepared electrode (ITO/PMT, ITO/PMT/Au-1 min, or ITO/PMT/Au-2 min) acts as the working electrode, while graphite and calomel are the counter and reference electrodes, respectively. The measurements were carried out from sewage water to electrolyte without using any additional electrolyte solution; then, these measurements were compared with Na₂S₂O₃ as a reference electrolyte. The measurements were carried out at room temperature (25 °C) under a 400 W artificial light, metal-halide lamp.

As shown in Figure 6a, the measurements were carried out in the dark and under light using the Na₂S₂O₃ electrolyte. The J_{ph} values are 0.0098, 0.12, and 0.33 mA cm⁻² at 1 V for electrodes ITO/PMT, ITO/PMT/Au-1 min and ITO/PMT/Au-2 min, respectively. This confirms the effect of Au nanoparticles on increasing the J_{ph} values. The Au plasmonic nanoparticles cause an increase in the electrode surface area; this process causes the light

capture and generates more electron-hole pairs on the surface of PMT, generating high J_{ph} values for H_2 generation under the water-splitting reaction.

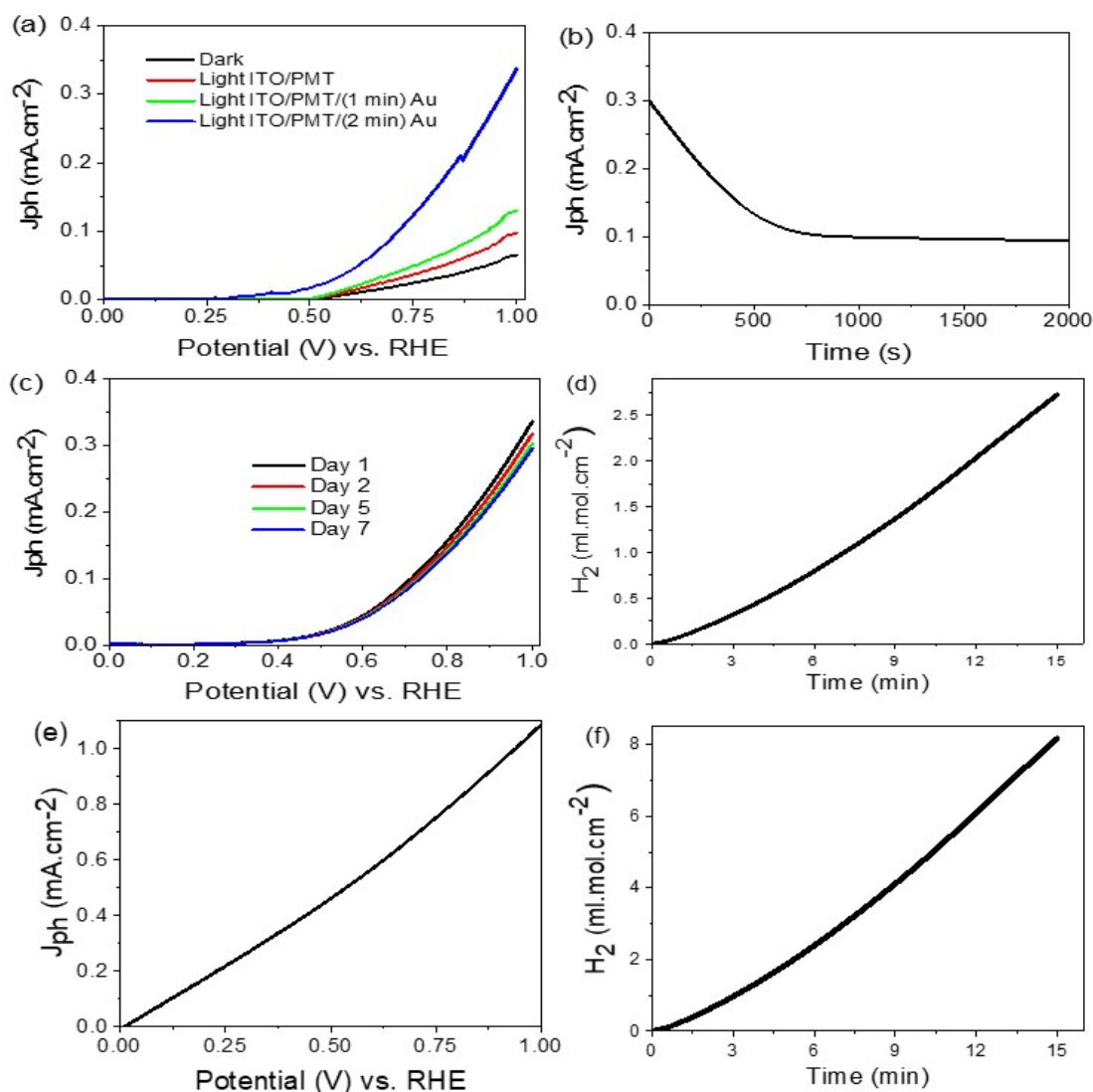


Figure 6. (a) Photocurrent voltage curves in dark (black) and under illumination for the ITO/PMT (red), ITO/PMT/Au-1 min (green), and ITO/PMT/Au-2 min (blue) electrodes; (b) current-time curve for the ITO/PMT/Au-2 min electrode at 0.75 V; (c) current-voltage characteristics for ITO/PMT/Au-2 min electrode under 7 days of illumination with a 400 W metal-halide lamp at 293 K; and (d) the evaluated H_2 moles at room temperature for ITO/PMT/Au-2 min using the $Na_2S_2O_3$ electrolyte. Sewage water (e) current-voltage characteristics for PMT/Au-2 min and (f) lifetime.

The small dark current density (J_0) for the ITO/PMT/Au-2 min electrode is related to the flow of electrons through the PMT and Au junction.

From this comparison using $Na_2S_2O_3$ as an electrolyte, ITO/PMT/Au-2 min electrode has the optimum behavior for the water splitting and H_2 generation process with the lowest photogeneration voltage (0.56 V).

The stability of the ITO/PMT/Au-2 min electrode was determined, at an applied bias voltage of 0.75 V, through the relation between the time and the produced J_{ph} values, as shown in Figure 6b. The produced J_{ph} values decrease smoothly from 0.3 to 0.1 $mA \cdot cm^{-2}$ on the first time and then become constant until reaching 2000 s. The decrease in the first period is related to the limited corrosion process in the electrode surface under the presence of the electrolyte [49]. The presence of Au nanoparticles protects the PMT layer

and decreases the corrosion behavior in this electrode. The stability and reproducibility of the electrode were measured for 7 days through the I–V relation, as shown in Figure 6c. The figure confirms the high stability of the electrode with time in relation to J_{ph} , which decreases only from 0.32 to 0.275 mA cm⁻² from the first to the seventh day, respectively.

The number of hydrogen mole was determined for the electrode, ITO/PMT/Au-2 min, by using the Na₂S₂O₃ electrolyte, as shown in Figure 6d. The hydrogen moles were calculated using Faraday's law (Equation (3)). This equation depends on the J_{ph} and time (dt) and the Faraday constant (F; 9.65×10^4 C mol⁻¹). The produced H₂ moles are 8.4 mmol/cm⁻² h; this hydrogen gas evolves as bubbles from the electrolyte, in which the Au nanoparticles enhance the number of moles evolved.

$$H_2(\text{moles}) = \int_0^t \frac{J_{ph} dt}{F} \cdot 1/2 \quad (3)$$

On the other hand, using the sewage water as an electrolyte without using any additional electrolyte is very promising for the H₂ generation reaction. The chemical construction of the sewage water is shown in Table 3. The J_{ph} value is enhanced after using the sewage water by the electrode PMT/Au-2 min, as shown in Figure 6e. The J_{ph} value reaches 1.09 mA cm⁻², which is an enhanced value compared with the previous standard electrolyte Na₂S₂O₃ that had a J_{ph} value of 0.33 mA cm⁻² (Figure 6a). Moreover, the number of the produced H₂ moles increased highly, as the produced H₂ moles reaches 33.1 mmol h⁻¹ cm⁻², as shown in Figure 6f.

Table 3. The chemical construction of sewage water.

Material or Element	Concentration (mg/L)
Phenols	0.015
F ⁻	1.0
Al ³⁺	3.0
NH ₃	5.0
Hg ²⁺	0.005
Pb ²⁺	0.5
Cd ³⁺	0.05
As ³⁺	0.05
Cr ³⁺	1.0
Cu ²⁺	1.5
Ni ³⁺	0.1
Fe ³⁺	1.5
Mn ²⁺	1.0
Zn ²⁺	5.0
Ag ⁺	0.1
Ba ³⁺	2.0
Co ²⁺	2.0
Other cations	0.1
Pesticides	0.2
CN ⁻¹	0.1
Industrial washing	0.5
Coli groups	4000/100 cm ³

The effect of temperature of 25–70 °C on the electrode ITO/PMT/Au-2 min for the water-splitting reaction and H₂ generation using the Na₂S₂O₃ electrolyte is shown in Figure 7a. The increasing in temperature from 25 to 70 °C causes the J_{ph} values to increase from 0.32 to 0.88 mA/cm², respectively, at 0.9 V. This is related to the role of the temperature in the increase in ion mobility and then the H₂ generation rate [50].

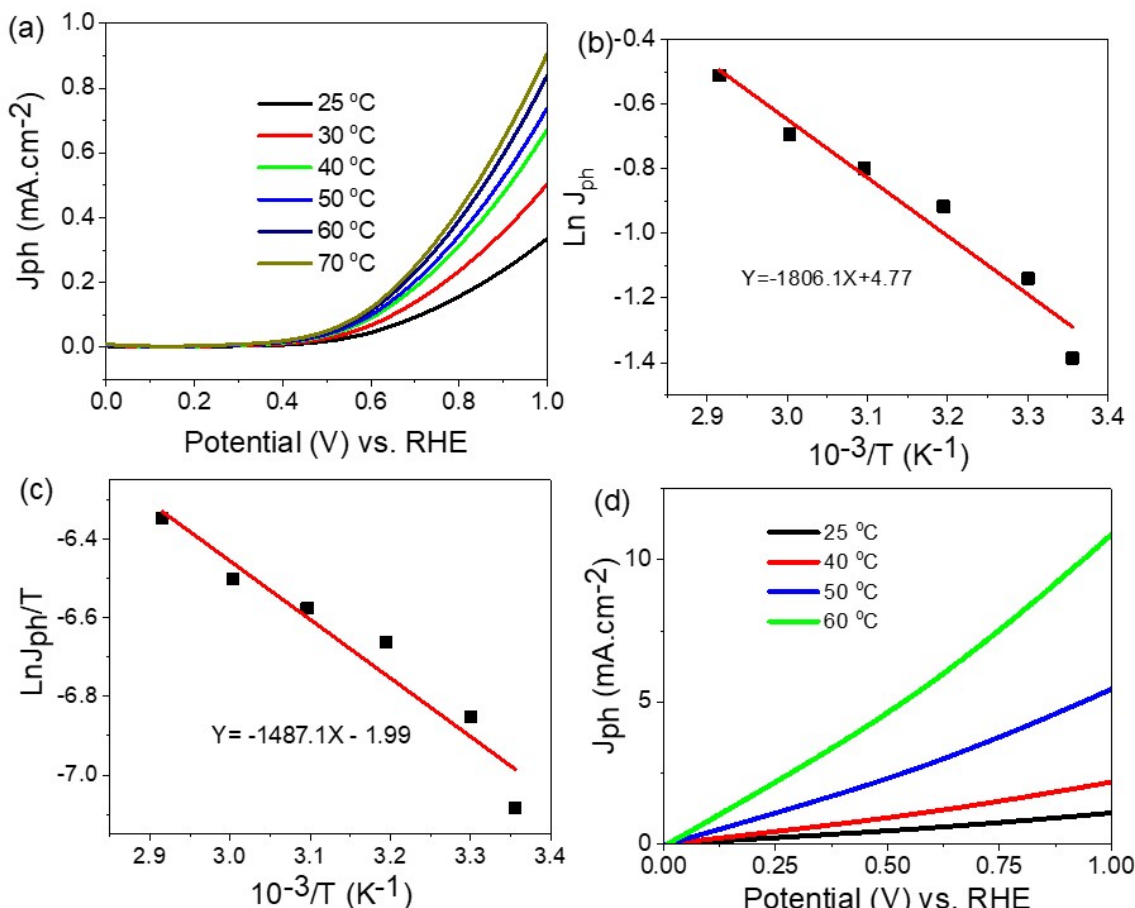


Figure 7. (a) The effect of the temperature on the produced J_{ph} value, (b) the Arrhenius relation, and (c) the Eyring relation for the PMT/Au-2 min electrode using the Na₂S₂O₃ electrolyte. (d) The effect of the temperature on the produced J_{ph} value for PMT/Au-2 min electrode using sewage water as the electrolyte.

The activation energy (E_a) can be calculated from the Arrhenius and Eyring equations, Equations (4) and (5), respectively [46,51]. These equations depend on the following factors: the Arrhenius constant (A), the universal gas constant (R), the temperature (T), the rate constant (k), the Boltzmann constant (B), and the Planck constant (h). From the Arrhenius equation and Figure 7b, the activation energy (E_a) is 31.49 KJ mol⁻¹.

$$k = Ae^{-E_a/RT} \tag{4}$$

The ΔH^* and ΔS^* values are calculated from the Eyring equation and Figure 7c, in which the values are 114.49 Jmol⁻¹ and 160.46 JK⁻¹ mol⁻¹, respectively:

$$k = T \cdot \frac{kB}{h} \cdot e^{\Delta S^*/R} \cdot e^{-\Delta H^*/RT} \tag{5}$$

On the other hand, after using the sewage water as an electrolyte, there is more enhancement in the produced J_{ph} values in comparison with the standard Na₂S₂O₃. The increase in temperature from 25 to 60 °C causes the J_{ph} values to increase from 1.09 to

11.2 mA cm⁻², respectively. This confirms the superiority of sewage water as an electrolyte for the water-splitting and H₂ generation reaction.

The effect of monochromatic light wavelengths between 390 and 636 nm on H₂ generation using the ITO/PMT/Au-2 min electrode is shown in Figure 8a. From this figure, the produced J_{ph} values decrease from 0.30 to 0.20 mA cm⁻², increasing the wavelengths from 390 to 500 nm, respectively. Then, the J_{ph} increases again until it reaches 0.28 mA cm⁻² at 636 nm. The wavelength 500 nm has the minimum J_{ph} value; this behavior is matched well with the optical absorbance spectrum in Figure 5A. Moreover, the good values of J_{ph} in the broad wavelength region confirm the solar absorption for the ITO/PMT/Au-2 min and H₂ generation in these light regions. Moreover, the Au nanoparticles play a good role in enhancing light absorption, and they overlap in the response of Au and PMT nanomaterials to produce J_{ph} values at lower potential.

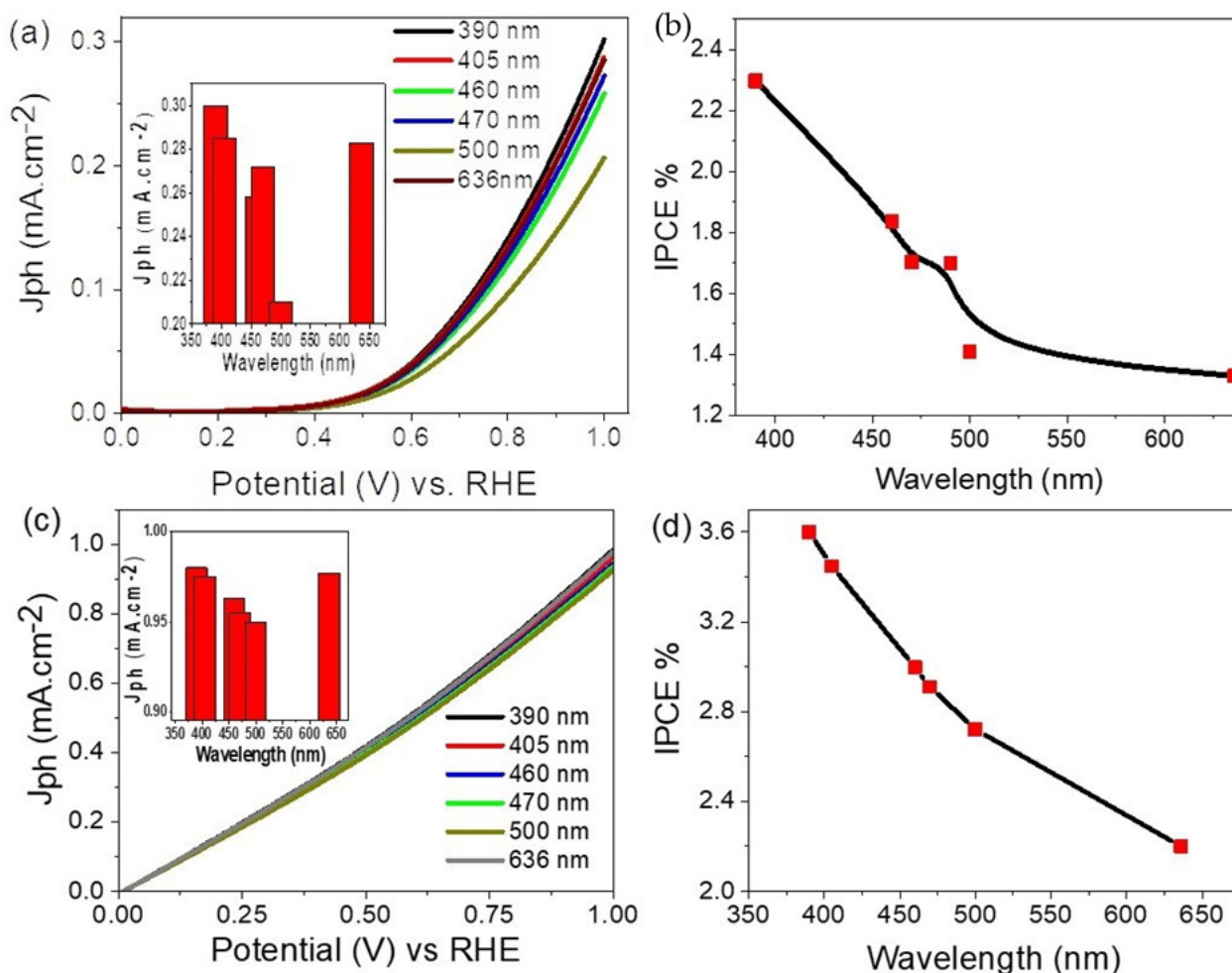


Figure 8. (a) The response of the PMT/Au-2 min electrode under different monochromatic light from 390 to 636 nm using electrolytes (a) $Na_2S_2O_3$ and (c) sewage water. The IPCE through using (b) $Na_2S_2O_3$ and (d) sewage water electrolyte.

Figure 8b represents the photon-to-current conversion efficiency (IPCE) for the electrode ITO/PMT/Au-2 min under the light for the water-splitting reaction and H₂ generation using the $Na_2S_2O_3$ electrolyte. This IPCE can be calculated using Equation (6) [52]. This equation depends on the J_{ph} , wavelength (λ) and light intensity (ρ). The IPCE value is 2.3% at 390 nm. These values are compared with the previous literature as shown in Table 4.

Table 4. IPCE and J_{ph} values of the present work compared with the previous literature.

Electrode Materials	Electrolyte	IPCE% (390 nm)	J_{ph} (mA cm ⁻²)
BiFeO ₃ [53]	Na ₂ SO ₄	–	0.16
Au/Pb(Zr,Ti)O ₃ [54]	Na ₂ SO ₄	–	0.06
CdSe/TiO ₂ nanotube electrode [55]	NaOH	0.45	0.13
Fe ₂ O ₃ /sodium dodecyl sulfonate electrodes [56]	NaOH	2	0.05
SnO ₂ /TiO ₂ [57]	Na ₂ S ₂ O ₃	–	0.4
ZnO/Ag [58]	Na ₂ SO ₄	0.5	1
PrFeO ₃ [59]	Na ₂ SO ₄	1.2	0.13
ITO/PMT/2 min-Au (present work)	Na ₂ S ₂ O ₃	2.3	0.3
ITO/PMT/2 min-Au (present work)	Sewage water	3.6	0.98

$$IPCE (\%) = 1240 \cdot \frac{J_{ph}}{\lambda \cdot \rho} \cdot 100 \quad (6)$$

Using sewage water as an electrolyte for H₂ generation using the electrode ITO/PMT/Au-2 min, there are more enhancements in the produced J_{ph} values as shown in Figure 8c. The variation of the produced J_{ph} values with the monochromatic light has the same behavior by using Na₂S₂O₃ as an electrolyte. The J_{ph} values decrease from 0.98 to 0.91 mA cm⁻², increasing the wavelength from 390 to 500 nm. Then, the J_{ph} value increases to 0.97 mA cm⁻² at 636 nm. The IPCE for the H₂ generation is 3.6%. These values are greater than the previous values by using the Na₂S₂O₃ electrolyte.

3.4. Mechanism

The prepared electrode PMT/Au-2 min mechanism for H₂ generation from Na₂S₂O₃ or sewage-water electrolyte was carried out using two steps; interfacial charge transfers take place due to the electron–hole transfer. In addition to the localized surface plasmonic resonance (LSPR), this process causes the oscillation of the electron on the surface of the semiconductor material. These two phenomena can appear well through the optical analyses (Figure 5A,B) and the electrochemical curve and H₂ moles produced (Figure 6a–f). Under the light incident, there is an electron transfer from the LUMO to HUMO for the PMT [60]; then, these electrons oscillate on the surface of the PMT and transfer the energy from the Au to PMT. The wide range of absorbance related to the PMT/Au composite increases the electron generation on the surface that is finally collected on the PMT surface under the LSPR process [61]. More electrons are generated with this high electromagnetic coupling between Au and PMT. Then, more H₂ generation reactions occur [62]. The electron transfer depends on the work function of Au and the electron affinity of PMT.

Moreover, the presence of the Schottky barrier limited the electron transfer under the presence of the internal electric field. This barrier push transfers the photoexcited electrons. At the same time, it prevents electron–hole pair recombination. This process causes an enhancement in the produced J_{ph} and then water splitting for the H₂ generation reaction [63]. The hot electrons pass to the PMT, while the cold electrons still suffer the internal barrier, as shown in Figure 9. Finally, these hot electrons are collected on the PMT surface for water splitting and H₂ generation reaction.

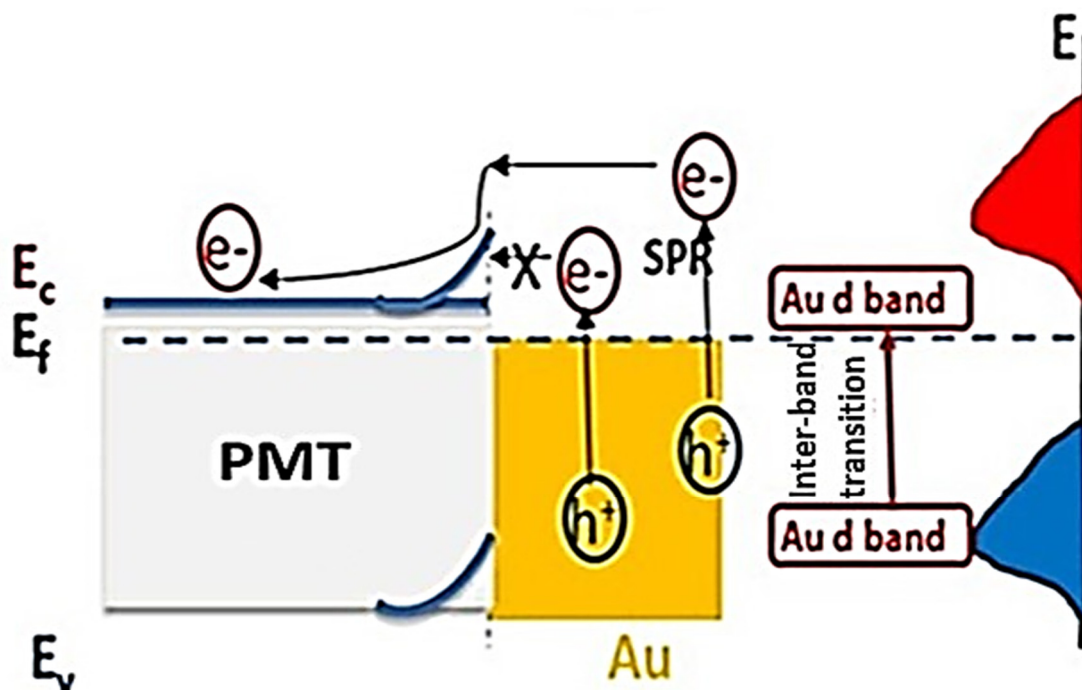


Figure 9. The mechanism of water splitting reaction using the PMT/Au-2 min electrode.

4. Conclusions

PMT preparation was carried out by the electropolymerization of m-toluidine on the ITO using the anodic polymerization method. Then, Au under different sputter coating times (0, 1, 2, and 3 min) was deposited on the PMT, in which the ITO/PMT, ITO/PMT/Au-1 min and ITO/PMT/Au-2 min electrodes were prepared. The full characteristic analyses were carried out to confirm the chemical structure and morphology of the prepared nano-materials. From the different analyses, the electrode ITO/PMT/Au-2 min has the optimum optical properties to be applied as an electrode for water splitting and H_2 generation. The thermodynamic parameters were calculated for the H_2 production from water using $Na_2S_2O_3$ as an electrolyte, in which E_a , ΔS^* , ΔH^* values were $31.49 \text{ kJ mol}^{-1}$, $160.46 \text{ JK}^{-1} \text{ mol}^{-1}$, and $114.49 \text{ J mol}^{-1}$, respectively. The electrode has high stability and reproducibility for H_2 generation reaction, in which the J_{ph} was decreased from 0.32 to 0.27 mA/cm^2 during the 7 days. The H_2 generation under sewage water splitting was carried out using the PMT/Au-2 min with high IPCE 3.6% at 390 nm, and the produced H_2 moles evolved were $33.1 \text{ mmol h}^{-1} \text{ cm}^{-2}$. These results were compared with the previous data of the $Na_2S_2O_3$ electrolyte with maximum IPCE 2.3% and H_2 moles of $8.4 \text{ mmol/cm}^2 \cdot \text{h}$.

We will continue this research by working on the synthesis of an electrochemical cell for sewage water splitting directly. Sewage water can be used as electrolyte inside the cell directly for H_2 gas production that is used as fuel inside homes, factories, and companies. This cell will be promising for renewable energy production, especially in remote regions, such as deserts and spacecraft.

Author Contributions: Conceptualization, A.A.A.A., N.M.A.H. and M.R.; methodology, software, validation, formal analysis, investigation, resources, data curation, writing—original draft preparation, visualization, supervision, and project administration, A.M.A., G.A.E.-F., A.A.A.A., M.R., M.S., N.C. and A.-H.I.M.; synthesization of the photoelectrode, A.M.A., G.A.E.-F., A.A.A.A. and M.R.; writing—review and editing, A.A.A.A., M.R., A.-H.I.M., M.A., M.R., N.C. and M.S.; funding, N.M.A.H., M.A. and A.-H.I.M. All authors have read and agreed to the published version of the manuscript.

Funding: This study is funded by Deanship of Scientific Research at Jouf University (DSR-2021-03-0316) and UAE University research program (#31N414).

Institutional Review Board Statement: The study was conducted in accordance with the Declaration of Helsinki, and approved by the Institutional Review Board.

Data Availability Statement: The data that support the findings of this study are available from the corresponding author upon reasonable request.

Acknowledgments: The authors extend their appreciation to: Deanship of Scientific Research at Jouf University (DSR-2021-03-0316) for funding this work, and the UAE University research program (#31N414).

Conflicts of Interest: The authors declare that they have no conflict of interest.

References

1. Brandt, J.; Salerno, F.; Fuchter, M.J. The added value of small-molecule chirality in technological applications. *Nat. Rev. Chem.* **2017**, *1*, 0045. [[CrossRef](#)]
2. Wade, J.; Hilfiker, J.N.; Brandt, J.R.; Liirò-Peluso, L.; Wan, L.; Shi, X.; Salerno, F.; Ryan, S.T.J.; Schöche, S.; Arteaga, O.; et al. Natural optical activity as the origin of the large chiroptical properties in π -conjugated polymer thin films. *Nat. Commun.* **2020**, *11*, 1–11. [[CrossRef](#)]
3. Worch, J. Stereochemical enhancement of polymer properties. *Nat. Rev. Chem.* **2019**, *3*, 514–535. [[CrossRef](#)]
4. Vøllestad, E.; Strandbakke, R.; Tarach, M.; Catalán-Martínez, D.; Fontaine, M.L.; Beeaff, D.; Clark, D.R.; Serra, J.M.; Norby, T. Mixed proton and electron conducting double perovskite anodes for stable and efficient tubular proton ceramic electrolyzers. *Nat. Mater.* **2019**, *18*, 752–759. [[CrossRef](#)] [[PubMed](#)]
5. Duan, C.; Kee, R.; Zhu, H.; Sullivan, N.; Zhu, L.; Bian, L.; Jennings, D.; O’Hayre, R. Highly efficient reversible protonic ceramic electrochemical cells for power generation and fuel production. *Nat. Energy* **2019**, *4*, 230–240. [[CrossRef](#)]
6. Service, R.F. New electrolyzer splits water on the cheap. *Science* **2020**, *367*, 80. [[CrossRef](#)]
7. Spitaleri, L.; Nicotra, G.; Zimbone, M.; Contino, A.; Maccarrone, G.; Alberti, A.; Gulino, A. Fast and Efficient Sun Light Photocatalytic Activity of Au/ZnO Core-Shell Nanoparticles Prepared by a One-Pot Synthesis. *ACS Omega* **2019**, *4*, 15061–15066. [[CrossRef](#)]
8. Hisatomi, T.; Domen, K. Reaction systems for solar hydrogen production via water splitting with particulate semiconductor photocatalysts. *Nat. Catal.* **2019**, *2*, 387–399. [[CrossRef](#)]
9. Shaban, M.; Rabia, M.; Eldakrory, M.G.; Maree, R.M.; Ahmed, A.M. Efficient photoelectrochemical hydrogen production utilizing of APbI₃ (A = Na, Cs, and Li) perovskites nanorods. *Int. J. Energy Res.* **2020**, *45*, 7436. [[CrossRef](#)]
10. Mohamed, F.; Rabia, M.; Shaban, M. Synthesis and characterization of biogenic iron oxides of different nanomorphologies from pomegranate peels for efficient solar hydrogen production. *J. Mater. Res. Technol.* **2020**, *9*, 4255–4271. [[CrossRef](#)]
11. Mohamed, S.H.; Zhao, H.; Romanus, H.; El-Hossary, F.M.; EL-Kassem, M.A.; Awad, M.A.; Rabia, M.; Lei, Y. Optical, water splitting and wettability of titanium nitride/titanium oxynitride bilayer films for hydrogen generation and solar cells applications. *Mater. Sci. Semicond. Process.* **2020**, *105*, 104704. [[CrossRef](#)]
12. Shaban, M.; Ali, S.; Rabia, M. Design and application of nanoporous graphene oxide film for CO₂, H₂, and C₂H₂ gases sensing. *J. Mater. Res. Technol.* **2019**, *8*, 4510–4520. [[CrossRef](#)]
13. Almohammed, A.; Shaban, M.; Mostafa, H.; Rabia, M. Nanoporous TiN/TiO₂/Alumina Membrane for Photoelectrochemical Hydrogen Production from Sewage Water. *Nanomaterials* **2021**, *11*, 2617. [[CrossRef](#)] [[PubMed](#)]
14. Elsayed, A.M.; Rabia, M.; Shaban, M.; Aly, A.H.; Ahmed, A.M. Preparation of hexagonal nanoporous Al₂O₃/TiO₂/TiN as a novel photodetector with high efficiency. *Sci. Rep.* **2021**, *11*, 17572. [[CrossRef](#)]
15. Rabia, M.; Shaban, M.; Adel, A.; Abdel-Khaliek, A.A. Effect of plasmonic Au nanoparticles on the photoactivity of polyaniline/indium tin oxide electrodes for water splitting. *Environ. Prog. Sustain. Energy* **2019**, *38*, 13171. [[CrossRef](#)]
16. Sharma, S.; Kumar, D.; Khare, N. Plasmonic Ag nanoparticles decorated Bi₂S₃ nanorods and nanoflowers: Their comparative assessment for photoelectrochemical water splitting. *Int. J. Hydrogen Energy* **2019**, *44*, 3538–3552. [[CrossRef](#)]
17. Shi, Y.; Wang, X.; Zhang, H.; Li, B.; Lu, H.; Ma, T.; Hao, C. Effects of 4-tert-butylpyridine on perovskite formation and performance of solution-processed perovskite solar cells. *J. Mater. Chem. A* **2015**, *3*, 22191–22198. [[CrossRef](#)]
18. Zhao, H.; Wu, M.; Liu, J.; Deng, Z.; Li, Y.; Su, B.L. Synergistic promotion of solar-driven H₂ generation by three-dimensionally ordered macroporous structured TiO₂-Au-CdS ternary photocatalyst. *Appl. Catal. B Environ.* **2016**, *184*, 182–190. [[CrossRef](#)]
19. Shaban, M.; Rabia, M.; El-Sayed, A.M.A.; Ahmed, A.; Sayed, S. Photocatalytic properties of PbS/graphene oxide/polyaniline electrode for hydrogen generation. *Sci. Rep.* **2017**, *7*, 1–13. [[CrossRef](#)]
20. Atta, A.; Abdelhamied, M.M.; Essam, D.; Shaban, M.; Alshammari, A.H.; Rabia, M. Structural and physical properties of polyaniline/silver oxide/silver nanocomposite electrode for supercapacitor applications. *Int. J. Energy Res.* **2021**; *accepted*. [[CrossRef](#)]
21. Sengodan, S.; Choi, S.; Jun, A.; Shin, T.H.; Ju, Y.W.; Jeong, H.Y.; Shin, J.; Irvine, J.T.S.; Kim, G. Layered oxygen-deficient double perovskite as an efficient and stable anode for direct hydrocarbon solid oxide fuel cells. *Nat. Mater.* **2015**, *14*, 205–209. [[CrossRef](#)] [[PubMed](#)]
22. Myung, J.H.; Neagu, D.; Miller, D.N.; Irvine, J.T.S. Switching on electrocatalytic activity in solid oxide cells. *Nature* **2016**, *537*, 528–531. [[CrossRef](#)]

23. Sayyah, E.-S.M.; Shaban, M.; Rabia, M. A sensor of *m*-cresol nanopolymer/Pt-electrode film for detection of lead ions by potentiometric methods. *Adv. Polym. Technol.* **2018**, *37*, 1296–1304. [[CrossRef](#)]
24. Sayyah, S.M.; Shaban, M.; Rabia, M. A sensor of *m*-toluidine/*m*-cresol polymer film for detection of lead ions by potentiometric methods. *Sens. Lett.* **2016**, *14*, 522–529. [[CrossRef](#)]
25. Jung, J.W.; Lee, C.L.; Yu, S.; Kim, I.D. Electrospun nanofibers as a platform for advanced secondary batteries: A comprehensive review. *J. Mater. Chem. A* **2016**, *4*, 703–750. [[CrossRef](#)]
26. Ognibene, G.; Gangemi, C.M.A.; Spitaleri, L.; Gulino, A.; Purrello, R.; Cicala, G.; Fragalà, M.E. Role of the surface composition of the polyethersulfone–TiP–H2T4 fibers on lead removal: From electrostatic to coordinative binding. *J. Mater. Sci.* **2019**, *54*, 8023–8033. [[CrossRef](#)]
27. Ghosh, S.; Kouamé, N.A.; Ramos, L.; Remita, S.; Dazzi, A.; Deniset-Besseau, A.; Beaunier, P.; Goubard, F.; Aubert, P.H.; Remita, H. Conducting polymer nanostructures for photocatalysis under visible light. *Nat. Mater.* **2015**, *14*, 505–511. [[CrossRef](#)]
28. Yin, Z.; Zheng, Q. Controlled synthesis and energy applications of one-dimensional conducting polymer nanostructures: An overview. *Adv. Energy Mater.* **2012**, *2*, 179–218. [[CrossRef](#)]
29. Modibane, K.D.; Waleng, N.J.; Ramohlola, K.E.; Maponya, T.C.; Monama, G.R.; Makgopa, K.; Hato, M.J. Poly(3-aminobenzoic acid) decorated with cobalt zeolitic benzimidazole framework for electrochemical production of clean hydrogen. *Polymers* **2020**, *12*, 1581. [[CrossRef](#)]
30. Xiao, K.; Tu, B.; Chen, L.; Heil, T.; Wen, L.; Jiang, L.; Antonietti, M. Photo-Driven Ion Transport for a Photodetector Based on an Asymmetric Carbon Nitride Nanotube Membrane. *Angew. Chemie Int. Ed.* **2019**, *58*, 12574–12579. [[CrossRef](#)]
31. Belabed, C.; Abdi, A.; Benabdelghani, Z.; Rekhila, G.; Etxeberria, A.; Trari, M. Photoelectrochemical properties of doped polyaniline: Application to hydrogen photoproduction. *Int. J. Hydrogen Energy* **2013**, *38*, 6593–6599. [[CrossRef](#)]
32. Mejia, E.; Cherupurakal, N.; Mourad, A.H.I.; Al Hassanieh, S.; Rabia, M. Effect of Processing Techniques on the Microstructure and Mechanical Performance of High-Density Polyethylene. *Polymers* **2021**, *13*, 3346. [[CrossRef](#)] [[PubMed](#)]
33. Sayyah, S.M.; Shaban, M.; Rabia, M. *m*-toluidine polymer film coated platinum electrode as a pH sensor by potentiometric methods. *Sens. Lett.* **2015**, *13*, 961–966. [[CrossRef](#)]
34. Sayyah, S.M.; El-Deeb, M.M.; Mohamed, A.S. Electrodeposition of poly(3-hydroxyaniline) from acidic aqueous/acetone solution. *Int. J. Polym. Mater. Polym. Biomater.* **2007**, *56*, 1079–1097. [[CrossRef](#)]
35. Sayyah, S.M.; Shaban, M.; Rabia, M. Electropolymerization of *m*-Toluidin on Platinum Electrode from Aqueous Acidic Solution and Character of the Obtained Polymer. *Adv. Polym. Technol.* **2018**, *37*, 126–136. [[CrossRef](#)]
36. Sayyah, S.M.; Shaban, M.; Rabia, M. A High-Sensitivity Potentiometric Mercuric Ion Sensor Based on *m*-Toluidine Films. *IEEE Sens. J.* **2016**, *16*, 1541–1548. [[CrossRef](#)]
37. Shaban, M.; Rabia, M.; Fathallah, W.; El-Mawgoud, N.A.; Mahmoud, A.; Hussien, H.; Said, O. Preparation and Characterization of Polyaniline and Ag/Polyaniline Composite Nanoporous Particles and Their Antimicrobial Activities. *J. Polym. Environ.* **2018**, *26*, 434–442. [[CrossRef](#)]
38. Schindler, A.; Neumann, G.; Rager, A.; Füglein, E.; Blumm, J.; Denner, T. A novel direct coupling of simultaneous thermal analysis (STA) and Fourier transform-infrared (FT-IR) spectroscopy. *J. Therm. Anal. Calorim.* **2013**, *113*, 1091–1102. [[CrossRef](#)]
39. Buda, S.; Nawój, M.; Mlynarski, J. Recent Advances in NMR Studies of Carbohydrates. *Annu. Rep. NMR Spectrosc.* **2016**, *89*, 185–223. [[CrossRef](#)]
40. Abukhadra, M.R.; Rabia, M.; Shaban, M.; Verpoort, F. Heulandite/polyaniline hybrid composite for efficient removal of acidic dye from water; kinetic, equilibrium studies and statistical optimization. *Adv. Powder Technol.* **2018**, *29*, 2501–2511. [[CrossRef](#)]
41. Shaban, M.; Abukhadra, M.R.; Rabia, M.; Elkader, Y.A.; Abd El-Halim, M.R. Investigation the adsorption properties of graphene oxide and polyaniline nano/micro structures for efficient removal of toxic Cr(VI) contaminants from aqueous solutions; kinetic and equilibrium studies. *Rend. Lincei. Sci. Fis. Nat.* **2018**, *29*, 141. [[CrossRef](#)]
42. Zhu, Q.; Liu, N.; Zhang, N.; Song, Y.; Stanislaus, M.S.; Zhao, C.; Yang, Y. Efficient photocatalytic removal of RhB, MO and MB dyes by optimized Ni/NiO/TiO₂ composite thin films under solar light irradiation. *J. Environ. Chem. Eng.* **2018**, *6*, 2724–2732. [[CrossRef](#)]
43. Contino, A.; Maccarrone, G.; Fragalà, M.E.; Spitaleri, L.; Gulino, A. Conjugated Gold–Porphyrin Monolayers Assembled on Inorganic Surfaces. *Chem.–A Eur. J.* **2017**, *23*, 14937–14943. [[CrossRef](#)]
44. Yeh, Y.C.; Creran, B.; Rotello, V.M. Gold nanoparticles: Preparation, properties, and applications in bionanotechnology. *Nanoscale* **2012**, *4*, 1871–1880. [[CrossRef](#)]
45. Thimsen, E.; Le Formal, F.; Grätzel, M.; Warren, S.C. Influence of plasmonic Au nanoparticles on the photoactivity of Fe₂O₃ electrodes for water splitting. *Nano Lett.* **2011**, *11*, 35–43. [[CrossRef](#)]
46. Peleg, M.; Normand, M.D.; Corradini, M.G. The Arrhenius equation revisited. *Crit. Rev. Food Sci. Nutr.* **2012**, *52*, 830–851. [[CrossRef](#)] [[PubMed](#)]
47. Rabia, M.; Mohamed, H.S.H.; Shaban, M.; Taha, S. Preparation of polyaniline/PbS core-shell nano/microcomposite and its application for photocatalytic H₂ electrogeneration from H₂O. *Sci. Rep.* **2018**, *8*, 1107. [[CrossRef](#)]
48. Evingür, G.A.; Pekcan, Ö. Optical energy band gap of PAAm–GO composites. *Compos. Struct.* **2018**, *183*, 212–215. [[CrossRef](#)]
49. Pan, L.; Liu, Y.; Yao, L.; Ren, D.; Sivula, K.; Grätzel, M.; Hagfeldt, A. Cu₂O photocathodes with band-tail states assisted hole transport for standalone solar water splitting. *Nat. Commun.* **2020**, *11*, 1–10. [[CrossRef](#)] [[PubMed](#)]

50. Helmy, A.; Rabia, M.; Shaban, M.; Ashraf, A.M.; Ahmed, S.; Ahmed, A.M. Graphite/rolled graphene oxide/carbon nanotube photoelectrode for water splitting of exhaust car solution. *Int. J. Energy Res.* **2020**, *44*, 7687–7697. [[CrossRef](#)]
51. Eyring, H. The activated complex in chemical reactions. *J. Chem. Phys.* **1935**, *3*, 63–71. [[CrossRef](#)]
52. Rabia, M.; Mohamed, S.H.; Zhao, H.; Shaban, M.; Lei, Y.; Ahmed, A.M. TiO₂/TiO_xN_y hollow mushrooms-like nanocomposite photoanode for hydrogen electrogeneration. *J. Porous Mater.* **2020**, *27*, 133–139. [[CrossRef](#)]
53. Kolivand, A.; Sharifnia, S. Enhanced photocatalytic hydrogen evolution from water splitting by Z-scheme CdS/BiFeO₃ hetero-junction without using sacrificial agent. *Int. J. Energy Res.* **2021**, *45*, 2739–2752. [[CrossRef](#)]
54. Wang, Z.; Cao, D.; Wen, L.; Xu, R.; Obergfell, M.; Mi, Y.; Zhan, Z.; Nasori, N.; Demsar, J.; Lei, Y. Manipulation of charge transfer and transport in plasmonic-ferroelectric hybrids for photoelectrochemical applications. *Nat. Commun.* **2016**, *7*, 1–8. [[CrossRef](#)] [[PubMed](#)]
55. Xiao, F.X.; Miao, J.; Wang, H.Y.; Yang, H.; Chen, J.; Liu, B. Electrochemical construction of hierarchically ordered CdSe-sensitized TiO₂ nanotube arrays: Towards versatile photoelectrochemical water splitting and photoredox applications. *Nanoscale* **2014**, *6*, 6727–6737. [[CrossRef](#)] [[PubMed](#)]
56. Taffa, D.H.; Hamm, I.; Dunkel, C.; Sinev, I.; Bahnemann, D.; Wark, M. Electrochemical deposition of Fe₂O₃ in the presence of organic additives: A route to enhanced photoactivity. *RSC Adv.* **2015**, *5*, 103512–103522. [[CrossRef](#)]
57. Sherman, B.D.; Ashford, D.L.; Lapidis, A.M.; Sheridan, M.V.; Wee, K.R.; Meyer, T.J. Light-Driven Water Splitting with a Molecular Electroassembly-Based Core/Shell Photoanode. *J. Phys. Chem. Lett.* **2015**, *6*, 3213–3217. [[CrossRef](#)]
58. Wei, Y.; Ke, L.; Kong, J.; Liu, H.; Jiao, Z.; Lu, X.; Du, H.; Sun, X.W. Enhanced photoelectrochemical water-splitting effect with a bent ZnO nanorod photoanode decorated with Ag nanoparticles. *Nanotechnology* **2012**, *23*, 235401. [[CrossRef](#)]
59. Freeman, E.; Kumar, S.; Thomas, S.R.; Pickering, H.; Fermin, D.J.; Eslava, S. PrFeO₃ Photocathodes Prepared Through Spray Pyrolysis. *ChemElectroChem* **2020**, *7*, 1365–1372. [[CrossRef](#)]
60. Feng, S.; Ji, W. Advanced Nanoporous Anodic Alumina-Based Optical Sensors for Biomedical Applications. *Front. Nanotechnol.* **2021**, *3*, 36. [[CrossRef](#)]
61. Langhammer, C.; Schwind, M.; Kasemo, B.; Zorić, I. Localized Surface Plasmon Resonances in Aluminum Nanodisks. *Nano Lett.* **2008**, *8*, 1461–1471. [[CrossRef](#)] [[PubMed](#)]
62. Chen, L.; Gu, Q.; Hou, L.; Zhang, C.; Lu, Y.; Wang, X.; Long, J. Molecular p–n heterojunction-enhanced visible-light hydrogen evolution over a N-doped TiO₂ photocatalyst. *Catal. Sci. Technol.* **2017**, *7*, 2039–2049. [[CrossRef](#)]
63. Elsayed, A.M.; Shaban, M.; Aly, A.H.; Ahmed, A.M.; Rabia, M. Preparation and characterization of a high-efficiency photoelectric detector composed of hexagonal Al₂O₃/TiO₂/TiN/Au nanoporous array. *Mater. Sci. Semicond. Process.* **2022**, *139*, 106348. [[CrossRef](#)]